Journal of Alloys and Compounds 843 (2020) 155902

Contents lists available at ScienceDirect

Journal of Alloys and Compounds

journal homepage: http://www.elsevier.com/locate/jalcom

Composition-driven crystal structure transformation and magnetic properties of electrodeposited Co–W alloy nanowires

Eunmin Yoo [a, 1], Aleksei Yu Samardak [b, 1], Yoo Sang Jeon [a], Alexander S. Samardak [b, c, **], Alexey V. Ognev [b], Sergey V. Komogortsev [d], Young Keun Kim [a, *]

[a] Department of Materials Science and Engineering, Korea University, Seoul, 02841, Republic of Korea
[b] School of Natural Sciences, Far Eastern Federal University, Vladivostok, 690950, Russia
[c] National Research South Ural State University, Chelyabinsk, 454080, Russia
[d] Institute of Physics, SB Russian Academy of Sciences, Krasnoyarsk, 660036, Russia

ARTICLE INFO

Article history:
Received 28 December 2019
Received in revised form
6 May 2020
Accepted 2 June 2020
Available online 9 June 2020

Keywords:
Co–W alloy
Nanowire
Electrodeposition
Crystal structure
Magnetic anisotropy
First-order reversal curve

ABSTRACT

The cobalt (Co)–tungsten (W) alloys exhibit unique combinations of mechanical and magnetic properties, biocompatibility, resistance against corrosion, wear, and high-temperature, which makes them desirable materials for various practical applications. A nanoporous template with incorporated Co–W alloy nanowires is a soft magnetic composite, whose dielectric and magnetic properties can be tuned through the host material, pore distribution and size, Co–W composition and crystal structure, and geometry of the nanowires. Here, we report the composition-dependent structural and magnetic properties of Co–W alloy nanowires embedded in alumina templates by electrodeposition. The addition of W transforms cobalt from the crystalline hexagonal-close-packed (hcp) Co to a mixed nanocrystalline/amorphous-like Co(W) solid solution with ferromagnetic behavior and composition similar to that of the weakly magnetic Co_3W compound. The combination of the approach to magnetic saturation, anisotropy field distribution method, micromagnetic simulations, and first-order reversal curve diagram identification method elucidates the structure-driven magnetization reversal processes in both individual nanowires and magnetostatically coupled array as a whole.

1. Introduction

Co–W alloys have attracted considerable interest because of their outstanding mechanical, tribological, and anticorrosion properties, high wear resistance, and ultralow degrees of cracking on various substrates [1–4]. Typically, owing to their corrosion resistance, Co–W alloys have been studied to replace Cr coatings for various applications in many industries such as the aircraft and automobile industries [5–7]. Contrary to the electrodeposition of Cr compounds, which produces a contaminated toxic waste causing critical health problems [5], the processing of Co–W is safe and environment-friendly. The Co–W alloys have been proposed as multi-function diffusion barrier materials for Cu metallization [8,9], cathodes for efficient hydrogen evolution [10], microbumps in microelectromechanical systems (MEMS) [4], and metamaterials for microwave tunable devices [11–13].

Elements such as W, Ge, Mo, and P have relatively negative cathodic deposition potentials and very low hydrogen overpotentials [4,14–16]. Therefore, pure W cannot be obtained alone from its aqueous solution by electrodeposition. However, when W is co-deposited with other metals such as Co, its alloys can be easily deposited up to a certain W content [7]. Co–W alloy films were synthesized by electrodeposition in the direct-current mode or pulsed-current mode [3,7,17–19]. Co–W alloy coatings were electrodeposited under different experimental conditions (e.g., at different pH values, concentrations of precursors, and current densities) [1,10,20–23]. The fabricated Co–W alloy films had various compositions and crystal-structure-dependent mechanical and magnetic properties. Few studies have been reported on Co–W alloy nanostructures such as mesowires [24], microbumps [25], nanolayers [9], and nanoparticles [4], where the dimensionalities

* Corresponding author.
** Corresponding author. School of Natural Sciences, Far Eastern Federal University, Vladivostok, 690950, Russia.
E-mail addresses: samardak.as@dvfu.ru (A.S. Samardak), ykim97@korea.ac.kr (Y.K. Kim).
[1] E. Yoo and A. Yu. Samardak contributed equally to this work.

https://doi.org/10.1016/j.jallcom.2020.155902

and spatial distributions of the nano-elements have important roles in addition to the crystal structures and compositions of the Co–W alloys. Co–W alloy nanowires (NWs) electrodeposited into nanoporous templates have also been investigated, though not extensively [4,26,27]. Detailed characterizations of the composition-dependent structural and magnetic properties of Co–W alloys at the nanoscale have not been carried out.

In this study, we synthesized arrays of Co and Co–W alloy NWs via electrodeposition by utilizing nanoporous alumina membranes. To control the composition of the Co–W alloy NWs, we changed the concentration of the electrolyte or applied current density. After the synthesis, we characterized the microstructure and magnetic properties according to the W content variation. In particular, we employed the first-order reversal curve (FORC) diagram method to elucidate the W-content-dependent magnetic anisotropy and magnetization reversal. The initial magnetization curves of the magnetic NWs were analyzed by using the approach to magnetic saturation and characterized under an applied magnetic field to estimate the macroscopic magnetic anisotropy. The magnetic hysteresis processes were analyzed through micromagnetic simulations considering the crystal structures, grain sizes, and spatial distributions of the Co–W NWs.

2. Experimental methods

The Co–W alloy NWs were synthesized by electrodeposition by employing anodized aluminum oxide (AAO) membranes (Top-membranes Technology), with a nominal pore diameter of 200 nm, as nanoporous templates. For the electrodeposition, a 300-nm-thick Ag layer was deposited as a cathode on one side of the template [28,29]. The citrate electrolyte contained cobalt sulfate heptahydrate ($CoSO_4 \cdot 7H_2O$), sodium tungstate dihydrate ($Na_2WO_4 \cdot 2H_2O$), sodium citrate tribasic dihydrate ($C_6H_7Na_3O_8$), boric acid (H_3BO_3), and citric acid ($C_6H_8O_7$). The bath temperature was maintained at 30 °C. Through the electrodeposition, Co–W alloy NWs were fabricated under constant current densities (1.25 and 5.0 mA/cm^2) measured by using a source meter (Keithley 2612B). The concentration and applied current density were adjusted to control the concentration of the Co–W alloy NWs. The electrodeposition is illustrated in Fig. 1(a–c). Also, each dimension of Fig. 1c is expressed in Fig. 1(d–f).

The morphologies of the alloy NWs were determined by field-emission scanning electron microscopy (FE-SEM, Hitachi SU-70) and high-resolution transmission electron microscopy (HR-TEM, JEOL JEM-2100F). The changes in microstructure according to the added amount of tungsten were evaluated by selected-area electron diffraction (SAED). The composition of the NWs was determined by inductively coupled plasma mass spectrometry (Agilent 7700).

The magnetization hysteresis loops of the template-assisted NWs in the AAO arrays were measured at room temperature by vibrating-sample magnetometry (VSM, Microsense EV9) up to the maximum magnetic field of ±20 kOe. To analyze the magnetization reversal processes, the magnetic hysteresis loops were measured at various angles and the angular dependencies of the coercive force and normalized remnant magnetization of the Co–W NWs were evaluated. The experimental results are supported by a micromagnetic simulation. Besides, the FORC-based identification method [30–32] was used with the help of additional measurements by using a separate VSM instrument (LakeShore 7410) to understand the distributions of the coercive forces and global and local magnetic interactions in the arrays of Co–W NWs with different microstructures.

3. Results and discussion

3.1. Microstructural characterization

As mentioned above, we changed the concentrations of the precursors and applied current density to control the composition of the Co–W alloy NWs, as shown in Table 1. The contents of the main species of tungsten forming compounds with Co increased with the concentrations of two precursors ($Na_2WO_4 \cdot 2H_2O$, $C_6H_7Na_3O_8$). Additionally, the increase in current density increased the W content in the Co–W alloy NWs.

Fig. 2 shows the morphologies and microstructures of the pure Co and Co–W alloy NWs. Cross-section FE-SEM images of the Co–W NWs embedded in the AAO membranes are shown in the insets of Fig. 2a, c, e. To precisely analyze the effects of the tungsten content on the magnetic properties, the lengths and diameters of the NWs were fixed to 5 μm and 200 nm, respectively. The inter-wire distance was 200 nm. Fig. 2b shows diffraction spots that indicate a textured crystalline structure of the hexagonal-close-packed-(hcp)-Co NWs with average grain sizes of 35–40 nm.

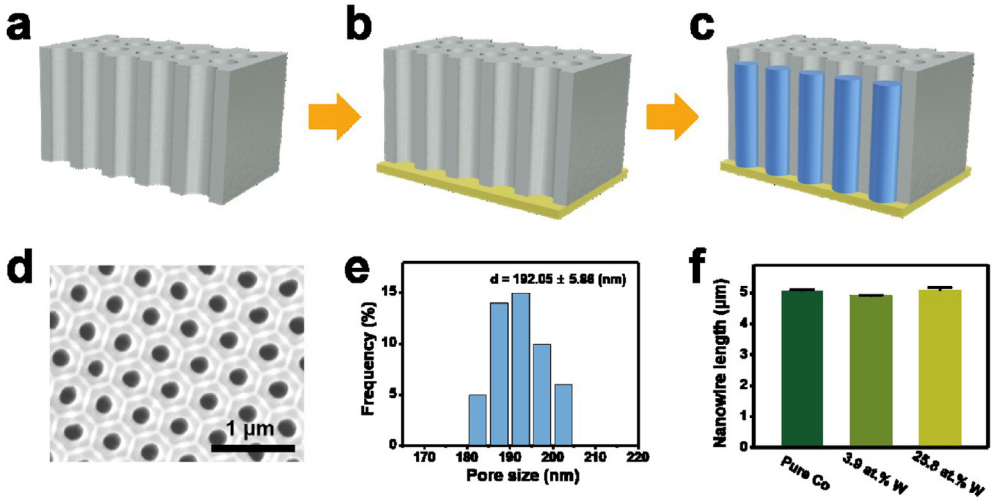

Fig. 1. Scheme of the electrodeposition including three basic steps: (a) fabrication of the AAO template, (b) deposition of the 300-nm-thick Ag cathode, and (c) electrodeposition of Co or Co–W. (d) A top view SEM image of AAO pores and (e) their size distribution. (f) Length distributions of nanowires with different W contents.

Table 1
Compositions of the Co–W NWs.

Current density (mA/cm^2)	Precursor-dependent content of W in the Co–W alloy (at%)		
	Na_2WO_4 (0.10 M)		Na_2WO_4 (0.20 M)
	$C_6H_7Na_3O_8$ (0.25 M)	$C_6H_7Na_3O_8$ (0.50 M)	$C_6H_7Na_3O_8$ (0.50 M)
1.25	3.9	6.9	22.0
5.00	14.3	17.0	25.8

When the amount of tungsten was increased to 3.9 at%, the SAED pattern (Fig. 2d) showed blurred reflections related to the polycrystalline structure with a less pronounced texture than that of the pure Co NWs. Fig. 2f presents the diffraction pattern of the Co–W alloy NWs having a W content of 25.8 at%, which is typical for a nanocrystalline or amorphous-like structure.

The interplanar distance $d(100)$ of the hcp phase determined by using the XRD data dependent on the tungsten content (Fig. 2g) obeys the Vegard's law for solid solutions (Fig. 3a). This demonstrates that the NW materials with W concentrations in the range of 0–14.3 at% are Co–W solid solutions. In the case of phase separation, the points would not be on the Vegard's line. This implies that all crystallites (grains) in the NWs, whose sizes were determined from the XRD patterns, consisted of dissolved hcp-Co–W phases, while the transition to the nanocrystalline state occurred at W contents larger than 17 at% (Fig. 3b). The reduction in the grain size is due to the incorporation of W, having a bigger atomic size, that refines the grain structure, increases the internal stresses, and introduces more lattice defects [1].

3.2. Coercivity, saturation magnetization, and macroscopic magnetic anisotropy of the Co–W NWs

Magnetic hysteresis loop measurements were carried out at room temperature to analyze the magnetization reversal, coercive force (H_c), and normalized remnant magnetization (M_r/M_s) depending on the angle (θ) between the main axis of the NWs and direction of the external magnetic field. At $\theta = 0°$, the magnetic field is parallel to the long axis of the NWs, while $\theta = 90°$ corresponds to the perpendicular orientation. Fig. 3c shows that the coercive force was very sensitive to the grain size of the Co–W alloy. The maximum H_c was obtained for the polycrystalline alloy having a grain size of approximately 30 nm. The transition to the nanocrystalline structure decreased H_c at least by one order of magnitude. The large decrease in H_c might be attributed to the switching of magnetization reversal modes, as presented in Section 3.4.

To assess the reliability of the saturation magnetization measurements of the Co–W alloys at room temperature, we summarize the literature data in Fig. 3d. The Fig. 3d contains the M_s values of all Co–W NWs estimated as $M_s = \langle H_a \rangle / 2\pi$, where $\langle H_a \rangle$ is the average magnetic anisotropy field determined by using the initial magnetization curve measured along the hard magnetization axis,

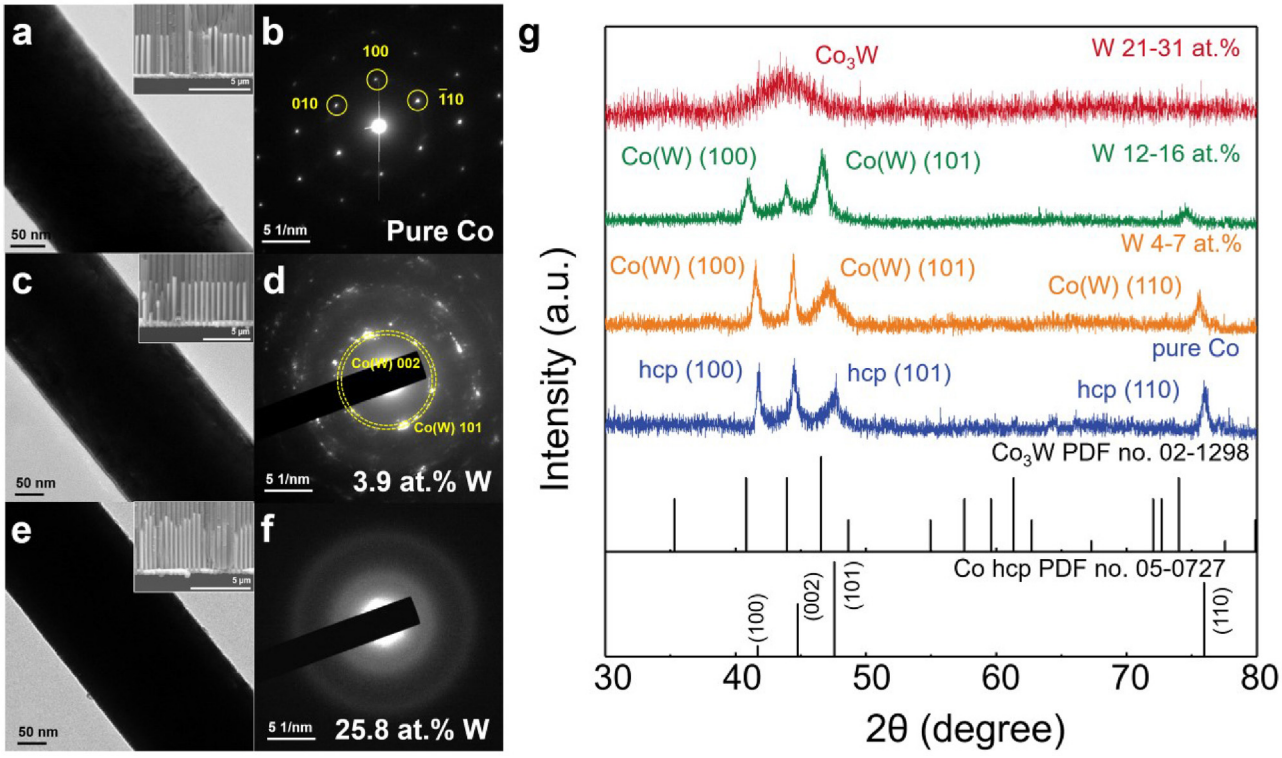

Fig. 2. (a, c, e) TEM images and (b, d, f) corresponding SAED patterns of the Co–W alloy NWs with tungsten contents of 0, 3.9, and 25.8 at%, respectively. (g) Composition-dependent X-ray diffraction (XRD) structural analysis of the Co–W alloy NWs.

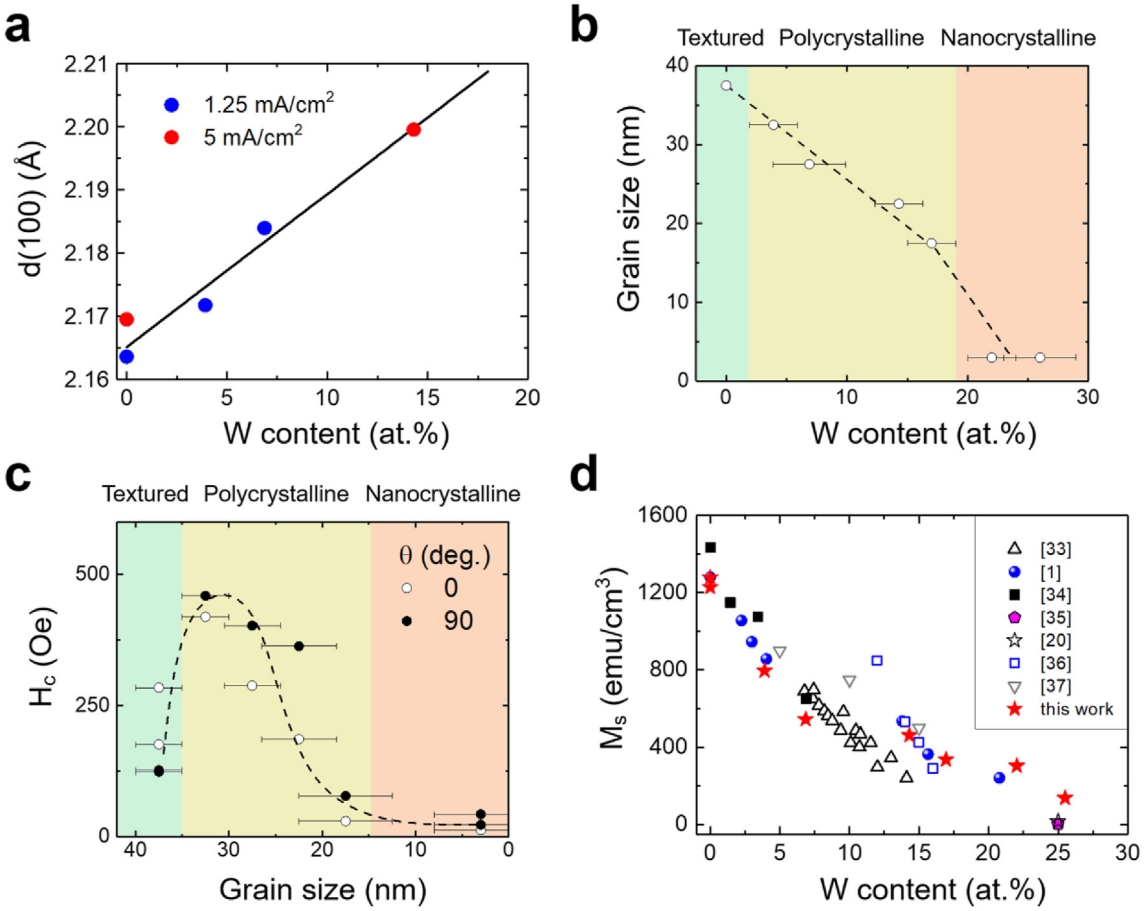

Fig. 3. (a) Linear dependence of the interplanar distance $d(100)$ on the W content for the NWs grown at different current densities of 1.25 and 5.0 mA/cm^2. (b) Grain size and crystal structure type variations depending on the W content. (c) Grain size dependences of the coercive force measured in two magnetic field geometries. (d) Saturation magnetizations of Co–W alloys measured in previous studies [1,20,33–37] and this study.

perpendicular to the main axis of the NWs (for a detailed explanation, see also Section 1 in Supplementary file). In this indirect method of M_s estimation, $\langle H_a \rangle$ is determined only by the shape anisotropy of the NWs. This assumption may be erroneous if other contributions to the magnetic anisotropy field exist, such as that by the texture of the crystallites. This explains M_s of the NWs consisting of pure Co, slightly smaller than 1400 emu/cm^3. According to the SAED patterns, the crystalline texture became weaker with the W addition and vanished at relatively large W contents (Fig. 3b). Thus, our estimation of M_s can be considered acceptable, particularly for W concentrations approaching 25 at%. Fig. 3d shows that M_s of the Co–W alloy NWs with the W content of 25.8 at% is slightly higher than those of films and coatings. Considering the broad XRD peak (Fig. 2g), it is difficult to distinguish a completely amorphous structure from a nanocrystalline structure with grain sizes of 1–3 nm. The SAED pattern of the Co–W NWs with the W content of 25.8 at% (Fig. 2f) contained not only a broad halo but also a low-intensity ring, which suggests that the sample was not completely amorphous and thus can be considered nanocrystalline.

The literature data in Fig. 3d demonstrate the trend in decreasing magnetization with the increase in W content. Likely, the large decrease in M_s at a W content of approximately 25 at% is attributed not to the complete formation line of the weakly magnetic crystalline Co_3W phase ($M_s \approx 15$ emu/cm^3), but to the transformation of the polycrystal structure to the nanocrystalline/amorphous-like structure, which is partially crystallized into the Co_3W phase ($M_s = 175$ emu/cm^3) [20]. The formation of such a mixed crystal phase could be attributed to the specific structural states at the grain boundaries. The Co–W alloy NWs with a composition similar to that of $Co_{75}W_{25}$ exhibit a saturation magnetization of 137 emu/cm^3 [20]. This suggests that the Co–W alloy with a W content of 25.8 at% consisted of this partially crystallized phase.

Fig. 4a shows the dependences of $\langle H_a \rangle$ on the W content (at%). The blue and red lines are in the W content range of 0–25 at%. At a W content of 0 at%, the magnetic anisotropy is set to correspond to NWs of pure cobalt with the same lengths, diameters, and distances between them as those observed in the SEM images (insets in Fig. 2a, c, and e). The magnetic anisotropy is primarily associated with the shape anisotropy, corrected for the dipole-dipole interaction in the NW array,

$$H_a = 2\pi M_s(1-3p)\left(1-x_{Co_3W}\right), \quad (1)$$

where p is the porosity factor and x_{Co_3W} is the volume fraction of Co_3W, which is weakly magnetic or even nonmagnetic [1,20,36–38]. The equilibrium phase diagram of Co–W [39] at given concentrations of W predicts a two-phase Co – Co_3W system. Equation (1) implies a linear decrease in the magnetization of such a system with the increase in W content.

However, as shown by the XRD patterns (Fig. 2g), a nonequilibrium solid solution Co(W) was formed during the electrodeposition. The partial separation into enriched and depleted W regions in this nonequilibrium system could explain the observed deviation

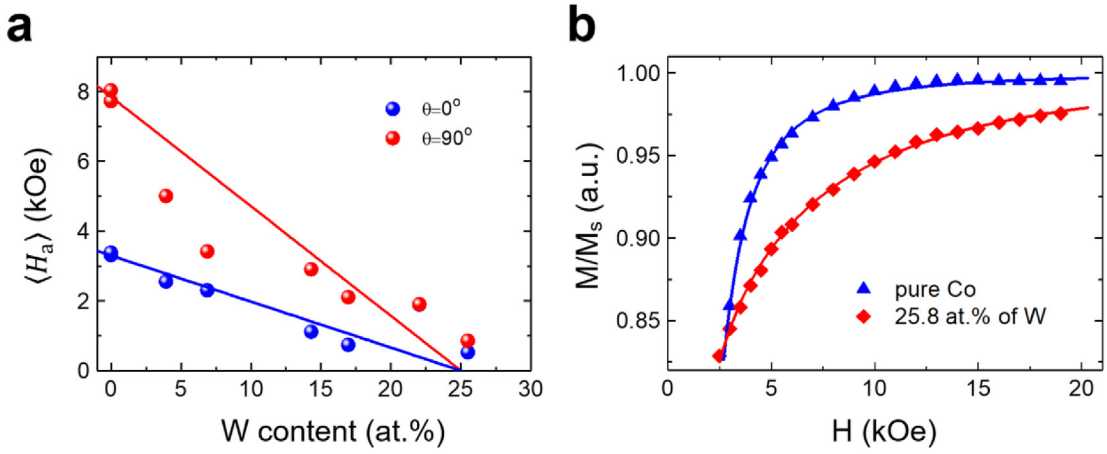

Fig. 4. (a) Macroscopic magnetic anisotropy fields H_a of the Co–W NWs estimated at different field orientations. (b) Fitting of high-field magnetization curves for the samples with W contents of 0 and 25.8 at%.

of the experimental points from the straight line in Fig. 4a. The XRD patterns show that the NWs with W contents larger than 20 at% consisted of amorphous-like Co(W) solutions with inclusions of nanocrystallites. This is consistent with the results of a previous study [36], where the amorphization at such concentrations was explained. The nanocrystalline/amorphous-like Co(W) was ferromagnetic, although it had the same concentration as that of the crystalline nonmagnetic Co_3W alloy. This explains the positions (above the line) of the red dots in Fig. 4a for W contents larger than 20 at%.

3.3. Local magnetic anisotropy in the Co–W NWs (approach to magnetic saturation)

To analyze the effect of the Co–W alloy composition on the local magnetic anisotropy, we utilized the approach to magnetic saturation, expressed by [40].

$$M(H) = \chi H + M_s\left(1 - \frac{(aH_a)^2}{H^{(4-d)/2}\left(H^{d/2} + {H_R}^{d/2}\right)}\right), \quad (2)$$

where the term χH reflects the paramagnetic contribution of the alumina membrane [32], H_R is the exchange field defined as $H_R = 2A/M_sR_c^2$, A is the exchange stiffness, R_c is the correlation length of the local easy magnetization axis, H_a is the local magnetic anisotropy field of the volume with a uniform orientation of the local easy axis, and d is the dimensionality of the magnetic anisotropy inhomogeneity.

Fig. 4b shows two examples of fitting of the high-field magnetization curves by using Equation (2) for the pure Co NWs and NWs with a W content of 25.8 at%. The fitting results of the approach to magnetic saturation are listed in Table 2.

Table 2
Fitting parameters of the high-field magnetization curves.

at% of W	d	H_a, kOe	H_R, kOe
0	0	4.33	–
0	0	3.62	–
3.9	0	3.63	–
6.9	0	5.34	–
14.3	3	7.09	4.6
17.0	3	6.39	2.2
22.0	3	4.76	3.6
25.8	3	13.7	12.0

The crystallites became smaller with the addition of tungsten, as evidenced by the XRD (001) peak broadening (Figs. 2g and 3b). Therefore, in the W content range of 6.9–14.3 at% (Table 2), the Co–W microstructure dimensionality d changed from 0 to 3. The corresponding crystal phase model was presented previously [32]. The anisotropy field H_a of the Co–W NWs is smaller than that of the hcp Co (H_a ~12 kOe), which may be attributed to structural defects (displaced planes). Surprisingly, the largest local magnetic anisotropy field was obtained for the nanocrystalline/amorphous-like ferromagnetic Co(W) having a composition similar to that of the crystalline weakly magnetic Co_3W (the magnetization of this sample was minimal).

3.4. Magnetization reversal modes of the Co–W alloy NWs

In the previous sections, we presented the characteristics of the crystal structures and their influences on the macro- and microscopic magnetic anisotropies. They are essential for better understanding of the magnetization reversal modes of the Co–W NWs depending on the W content. Fig. 5 shows the angular dependences of H_c and M_r/M_s. The W content largely influenced the H_c and M_r/M_s behaviors. The various H_c behaviors suggest different magnetization reversal modes [41]. In the pure hcp Co, the preferred reversal mode is transverse domain wall nucleation and propagation [42]. A small addition of W led to a change in reversal mode, which can be attributed to the curling of magnetization inducing vortex domain walls [28]. The very small (smaller than 0.15) values of M_r/M_s (Fig. 5b) reflect the practically complete self-demagnetization of the samples after the external magnetic field was switched off. Analytical calculations of the reversal modes for pure Co NWs are presented in our previous report [28]. However, the analytical and experimental results for the Co–W NWs do not agree, because the analytical model is qualitative and does not consider the crystal structure characteristics [42–44].

A micromagnetic simulation was carried out to understand the micromagnetic origin of the hysteretic processes. We used a hexagonal lattice with a central node formed by seven parallel NWs with parameters corresponding to the experimentally determined parameters. The cell dimensions were set to 10 × 10 × 10 nm^3. Based on the structural analysis, the hcp Co(100) axis was set to coincide with the easy magnetization axis. In the first approximation, the micromagnetic model of an NW can be represented by grains in the form of discs with thicknesses equal to the sizes of the

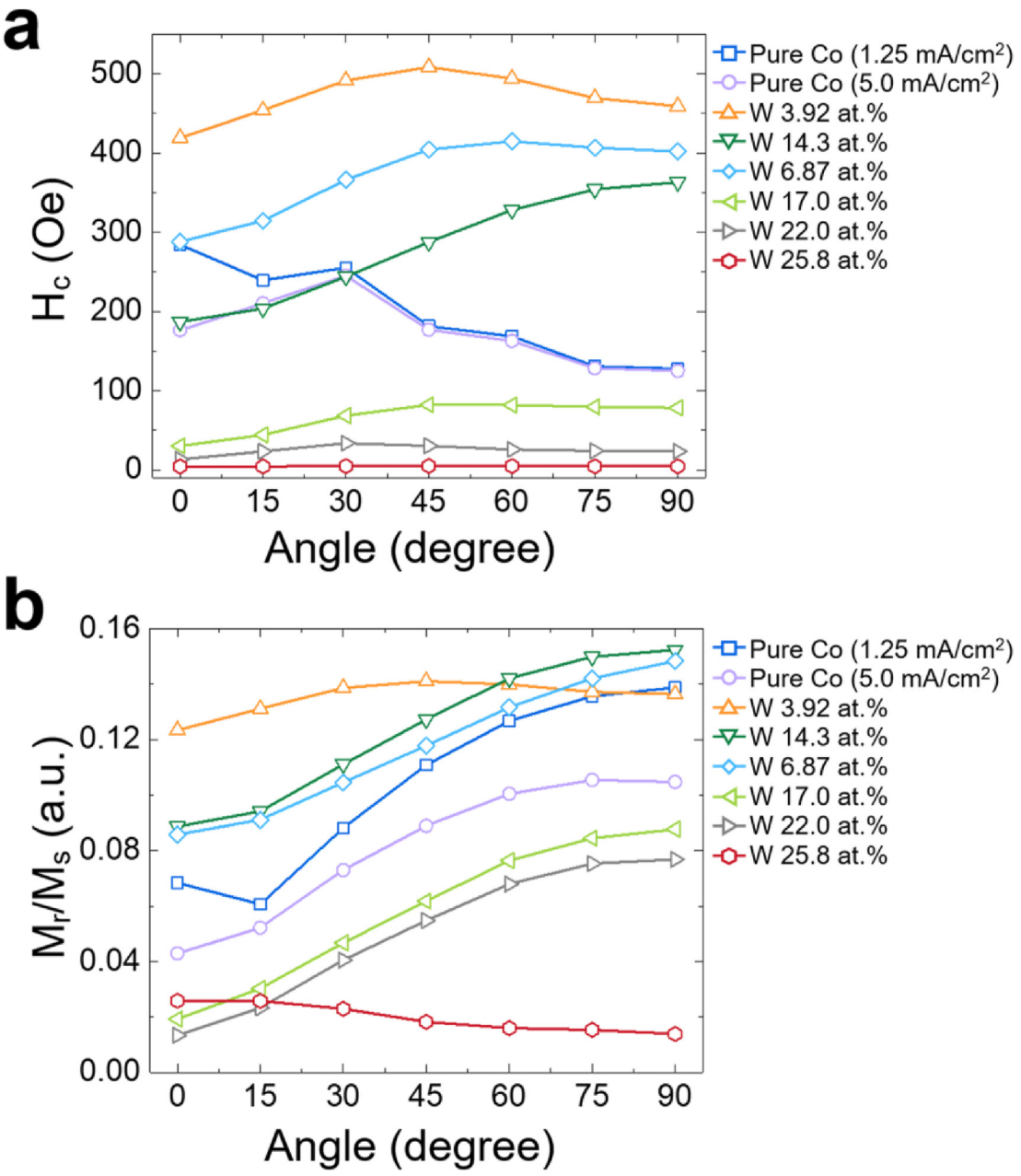

Fig. 5. Angular dependences of (a) H_c and (b) M_r/M_s of the Co–W alloy NWs with the different contents of W.

crystallites (38 nm in this case). The easy magnetization axis was in the plane of the discs (i.e., perpendicular to the long axis of the NW). However, the easy axis was randomly oriented in the disc plane in the different disks as no preferential axis direction in the individual disc's plane existed. The saturation magnetization of the Co(W) solid solution was smaller than that of the pure Co and decreased with the increase in W content. For the pure Co NWs, we used the experimentally determined saturation magnetization (M_S = 1276 emu/cm^3, Fig. 3d), exchange stiffness A of 3.0×10^{-6} erg/cm, and magnetocrystalline anisotropy constant K_1 of 3.0×10^6 erg/cm^3, smaller than that of the monocrystalline Co, because of possible structural defects and impurities.

Fig. 6a presents experimental and modeled hysteresis loops for the two orientations of the external magnetic field. The best agreement was achieved for the parallel orientation to the main NW axis ($\theta = 0°$). The magnetization reversal in this geometry was caused by the sequence of transverse and vortex domain wall nucleation and propagation along the NW axis, which led to the complete magnetization switching in the opposite saturation magnetic field [45]. In the perpendicular geometry ($\theta = 90°$), not only coherent rotation of magnetization in some grains but also a sequence of the vortex and transverse domain walls were observed. The intergrain exchange interaction had a significant role leading to the antiferromagnetic-like ordering of local magnetizations in adjacent disc-shaped crystallites. At zero field, this exchange interaction contributed to the decrease in remnant magnetization. The detailed magnetization processes defined from micromagnetic simulations for both geometries are presented in the Supplementary file (Section 2, Tables S2 and S3).

Fig. 6b shows experimental and simulated hysteresis loops of the Co–W NWs with a W content of 14.3 at%. In this case, we used the same geometry for the micromagnetic simulation, but the grain

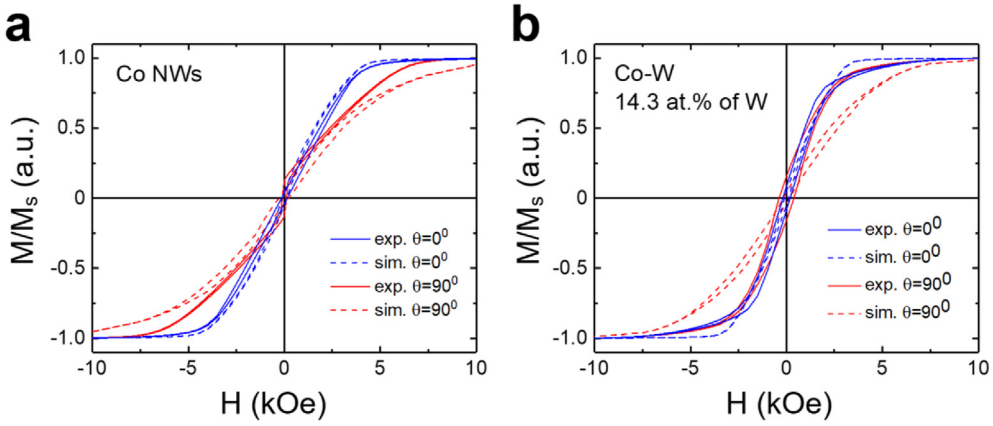

Fig. 6. Experimental and simulated magnetic hysteresis loops of the (a) Co and (b) Co–W NWs.

size was decreased to 23 nm according to the XRD results. M_s was 458 emu/cm^3, while $K_1 = 2.0 \times 10^6$ erg/cm^3. The observed magnetization reversal processes were very similar to those in the pure Co NWs, discussed above. As shown in Fig. 6b, the modeled loop at $\theta = 0^\circ$ coincided with the experimental data, both qualitatively (characteristic switching processes caused by Barkhausen jumps (for switching interacting NW segments in different fields)) and quantitatively (the coercive forces and saturation fields were almost equal). On the other hand, the loops at $\theta = 90^\circ$ differed qualitatively (avalanche-like reversal process instead of the coherent rotation observed in the experiment) and quantitatively (the saturation field was considerably larger than the experimental value), which can be associated with the small number of simulated NWs in the array.

3.5. FORC analysis

By using the FORC diagram identification method [46,47], we carried out qualitative and quantitative analyses of the Co–W alloy NW array according to the W content (Fig. 7). We expected that the samples with smaller W contents exhibit higher M_s values and consequently larger dipolar couplings between adjacent NWs in the array. The strong dipolar coupling even in the diluted NWs in the absence of an external magnetic field can induce the antiparallel alignment of magnetizations in adjacent NWs, which leads to a net magnetization of the array close to zero, as observed in the experiment (Fig. 5b). However, the micromagnetic simulations showed that the intergrain exchange interaction can be another factor for the self-demagnetization of individual NWs, which leads to zero net magnetization of the whole array.

The method of FORC diagrams is based on the measurement of a set of minor hysteresis loops, where each curve begins with a start field H_r. H_r varies with a certain step, from the positive saturation field + H_s to the negative field -H_s. The result is a set of FORCs, 70–100 curves with individual values of H_r and H, which is the field at which the magnetic moment (m) was measured. The FORC distribution $\rho(H, H_r)$ can be defined as the family of mixed derivatives of the second-order obtained from $m(H, H_r)$,

$$\rho(H, H_r) = -\frac{1}{2}\left[\frac{\partial^2 m(H, H_r)}{\partial H \partial H_r}\right] \quad (3)$$

We used a new set of coordinates (H_c, H_u), defined as $H_c = \frac{(H - H_r)}{2}$ and $H_u = \frac{(H + H_r)}{2}$. Thus, the FORC distributions were rotated by 45°, as shown in Fig. 7.

The FORC diagram of the pure Co NWs along their main axis shows typical results for strongly coupled interacting uniaxial NWs with a high magnetic moment (Fig. 7a) [28]. For quantitative analysis, we extracted the coercive forces (H_c^F) as the maximum values of the ridges along the H_c axis at $H_u = 0$. The interaction field at saturation (ΔH_u) can be defined as the half-width of the H_u distribution along the H_u axis at H_c^F. Considering the wide distribution of the interaction field $\Delta H_u = 3220$ Oe, irreversible processes occur for the whole set of curves, from $H_r = 3500$ Oe to −4000 Oe. This implies that the individual NW switching begins at very high fields owing to the strong coupling between the NWs. The main peak of the pure Co is located at $H_c^F = 418$ Oe, while the coercive force derived from the hysteresis loop is $H_c^h = 142$ Oe, which can be related to the switching of dipolarly coupled NWs. The emergence of the tail along the H_c axis, with a second standalone coercivity peak at $H_c^F = 1010$ Oe almost without shift along the H_u axis, implies a second relatively significant switching process related to a weakly interacting phase with a larger coercivity. This can be attributed to (i) growth of a Co film on the surface of the AAO template or (ii) different orientations of the easy magnetization crystallographic axes of the hcp Co phase. Another significant characteristic of this image is the rather weak peak distributed nearby the $H_c = 0$ Oe axis, but at high interaction fields ($H_u = -3100$ and 3600 Oe) (Fig. 7a). It can be originated from magnetic dendrites at the bottom of the NWs [48], where the magnetization is affected by the mean-field of the whole array.

The FORC diagram of the Co NWs in the direction perpendicular to the NW main axis ($\theta = 90^\circ$, Fig. 7b) shows almost no irreversible component. This suggests the only coherent rotation of magnetic vectors without switching peak in the majority of starting fields H_r. Such behavior can represent the coherent rotation of the magnetization in the whole NW array.

With the addition of W, the FORC diagrams change considerably, as shown in Fig. 7c and d. The shape of the FORC diagram of the Co–W NWs with the W content of 3.9 at% measured at $\theta = 0^\circ$ is significantly transformed to a wider coercive force distribution and long "tail" along the H_c axis. The increase in H_c distribution occurs possibly owing to the increase in dispersion of crystallite sizes. ΔH_u decreases twice, which can be related to the increasing concentration of W atoms in the intergrain boundaries and the reducing crystallite sizes and magnetic moment of the Co–W compound compared to pure Co NWs.

The further increase in W content leads to reversible magnetization processes of the magnetically soft phase at $H_c = 0$ and separate peak at $H_c = 2100$ Oe corresponding to the magnetically hard phase originated from the significant structural transformation (Fig. 7e). The origin of the soft magnetic phase can be

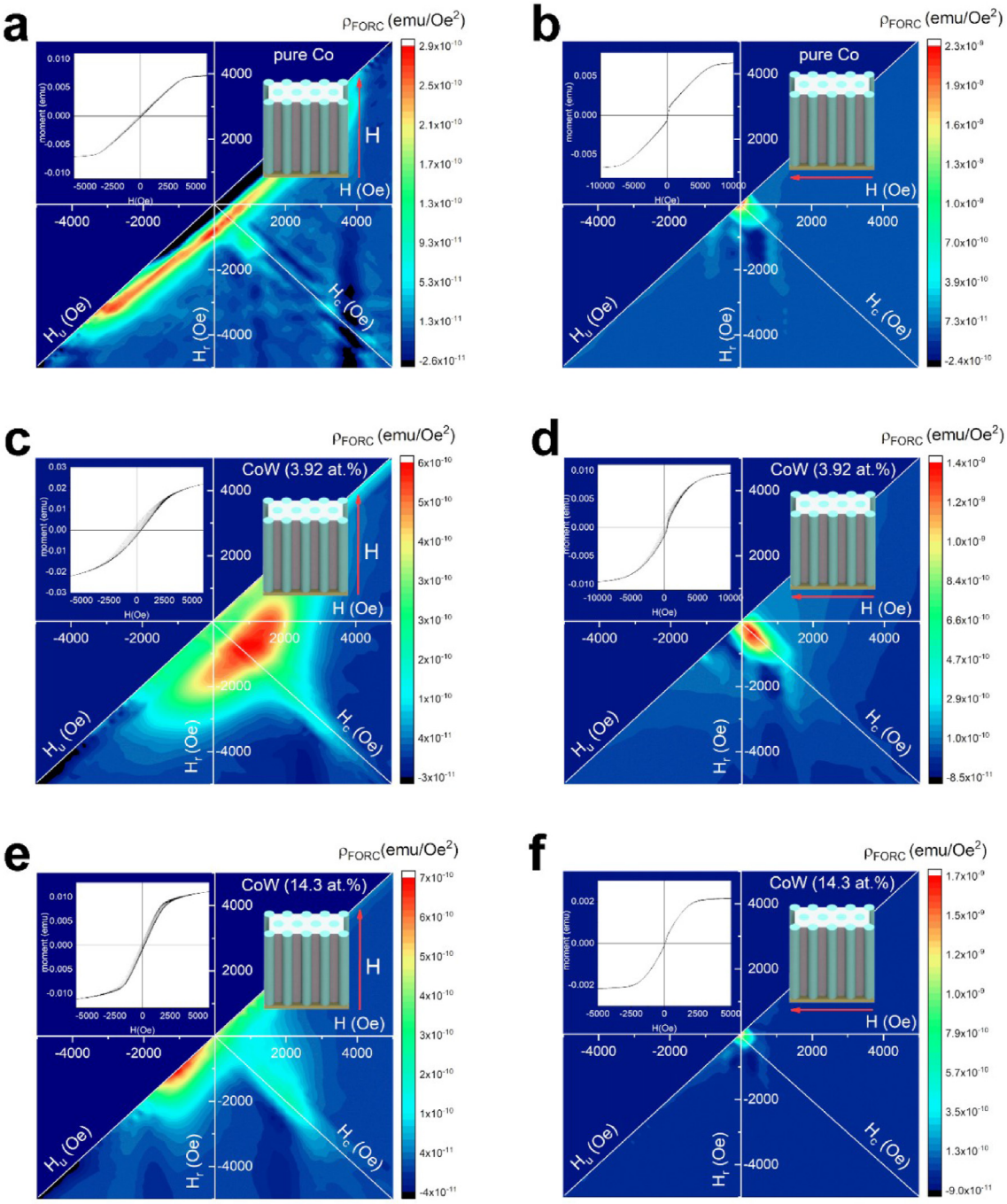

Fig. 7. FORC diagrams of the NWs with W contents of (a, b) 0, (c, d) 3.9, and (e, f) 14.3 at%. The red arrow in each inset indicates the direction of the applied magnetic field. (For interpretation of the references to colour in this figure legend, the reader is referred to the Web version of this article.)

attributed to the gradual transformation of the polycrystalline Co–W alloy to a ferromagnetic nanocrystalline/amorphous-like Co(W-rich) solid solution, as discussed in Section 3.2. The relatively hard magnetic phase can be formed by the NWs or their parts consisting of ultrafine Co-rich grains separated by intergranular boundaries filled by amorphous W. The parameters derived from the FORC diagrams for all samples are shown in Table S4 of Supplementary file. Some table cells are empty owing to the specificity of the FORC diagrams. The FORC diagrams of the samples with W contents of 6.9, 17, 22, and 25.8 at% are presented in the Supplementary file (Section 3, Figs. S3–S6). The transformation of the crystal structure was enhanced in the samples with W contents above 17 at%. This reduced the influence of the crystal structure on the magnetization reversal processes. As shown in Supplementary file, for the Co–W NWs with the W content of 25.8 at% and hybrid nanocrystalline/amorphous-like structure, the reversible processes became dominant, while the magnetostatic interaction between NWs was still not negligible (Table S4 in Supplementary file).

4. Conclusions

In this study, we fabricated a series of Co–W alloy NW arrays with different concentrations of W in the range of 0–25.8 at%. The combination of structural analysis and magnetic characterization

demonstrated that the W addition led to the gradual nanocrystallization and partial amorphization of the alloy. Notably, at W contents larger than 20 at%, the hybrid nanocrystalline/amorphous-like Co(W) solid solution was formed. Although the crystalline Co_3W alloy with the same concentration of W is weakly magnetic, the nanocrystalline Co(W) solution was ferromagnetic and exhibited the largest local magnetic anisotropy field. The structural transformations modified the micromagnetic structure of the Co–W NWs, which was the main driver of magnetization reversal processes not only in an individual NW but also in the NW array as a whole. The length distribution of the NWs within ±10% was the main origin of the coercive and anisotropy field distributions. The micromagnetic simulations and FORC diagram interpretation method demonstrated the self-demagnetization of the NW arrays by inter- and intra-nanowire magnetostatic interactions.

CRediT authorship contribution statement

Eunmin Yoo: Investigation, Data curation, Visualization, Writing - original draft. **Aleksei Yu Samardak:** Investigation, Data curation, Visualization. **Yoo Sang Jeon:** Methodology, Resources, Visualization. **Alexander S. Samardak:** Validation, Formal analysis, Visualization, Funding acquisition, Writing - original draft, Writing - review & editing. **Alexey V. Ognev:** Formal analysis, Supervision. **Sergey V. Komogortsev:** Methodology, Formal analysis, Visualization. **Young Keun Kim:** Conceptualization, Project administration, Supervision, Funding acquisition, Writing - review & editing.

Declaration of competing interest

The authors declare that they have no known competing financial interests or personal relationships that could have appeared to influence the work reported in this paper.

Acknowledgments

This study was supported by the Samsung Research Funding & Incubation Center of Samsung Electronics under Project Number SRFC-TA1703-06, and by the Russian Ministry of Science and Higher Education under the state task (0657-2020-0013), by Act 211 of the Government of the Russian Federation (02.A03.21.0011).

Appendix A. Supplementary data

Supplementary data to this article can be found online at https://doi.org/10.1016/j.jallcom.2020.155902.

References

[1] N. Tsyntsaru, H. Cesiulis, E. Pellicer, J.-P. Celis, J. Sort, Structural, magnetic, and mechanical properties of electrodeposited cobalt–tungsten alloys: intrinsic and extrinsic interdependencies, Electrochim. Acta 104 (2013) 94–103, https://doi.org/10.1016/j.electacta.2013.04.022.
[2] U. Admon, M. Dariel, E. Grünbaum, Microstructure of electrodeposited Co-W thin films, J. Appl. Phys. 59 (1986) 2002–2009, https://doi.org/10.1063/1.336380.
[3] N. Tsyntsaru, H. Cesiulis, A. Budreika, X. Ye, R. Juskenas, J.-P. Celis, The effect of electrodeposition conditions and post-annealing on nanostructure of Co–W coatings, Surf. Coating. Technol. 206 (2012) 4262–4269, https://doi.org/10.1016/j.surfcoat.2012.04.036.
[4] N. Tsyntsaru, Electrodeposition of cobalt–tungsten alloys and their application for surface engineering, Russ. J. Electrochem. 52 (2016) 1041–1047, https://doi.org/10.1134/S1023193516110136.
[5] A. Bodaghi, J. Hosseini, Corrosion behavior of electrodeposited cobalt-tungsten alloy coatings in NaCl aqueous solution, Int. J. Electrochem. Sci. 7 (2012) 2584–2595.
[6] L. Ma, X. Xi, Z. Nie, T. Dong, Y. Mao, Electrodeposition and characterization of Co-W alloy from regenerated tungsten salt, Int. J. Electrochem. Sci. 12 (2017) 1034–1051, https://doi.org/10.20964/2017.02.37.
[7] N. Tsyntsaru, H. Cesiulis, M. Donten, J. Sort, E. Pellicer, E. Podlaha-Murphy, Modern trends in tungsten alloys electrodeposition with iron group metals, Surf. Eng. Appl. Electrochem. 48 (2012) 491–520, https://doi.org/10.3103/S1068375512060038.
[8] Y.-H. Su, J.-N. Shih, Y.-S. Wang, W.-H. Tseng, W.-H. Liao, C.-Y. Hung, W.-H. Lee, Y.-L. Wang, CoW alloy as multi-function diffusion barrier material for next-generation Cu metallization, in: 2015 International Symposium on Next-Generation Electronics (ISNE), IEEE, 2015, pp. 1–3, https://doi.org/10.1109/ISNE.2015.7132035.
[9] N. Tsyntsaru, S. Belevsky, H. Cesiulis, A. Dikusar, J.-P. Celis, Cu/Co-W nanolayers electrodeposited from single bath and investigations of their nanohardness, Surf. Eng. Appl. Electrochem. 48 (2012) 418–425, https://doi.org/10.3103/S1068375512050134.
[10] E. Vernickaite, N. Tsyntsaru, K. Sobczak, H. Cesiulis, Electrodeposited tungsten-rich Ni-W, Co-W and Fe-W cathodes for efficient hydrogen evolution in alkaline medium, Electrochim. Acta 318 (2019) 597–606, https://doi.org/10.1016/j.electacta.2019.06.087.
[11] J. De La Torre Medina, J. Spiegel, M. Darques, L. Piraux, I. Huynen, Differential phase shift in nonreciprocal microstrip lines on magnetic nanowired substrates, Appl. Phys. Lett. 96 (2010), 072508.
[12] J. Wang, Z. Peng, J.-F. Lee, Ferromagnetic nanowires: homogenization and applications, URSI Radio Science Bulletin 2014 (2014) 40–51, https://doi.org/10.1063/1.3313942.
[13] M. Darques, J. Spiegel, J. De la Torre Medina, I. Huynen, L. Piraux, Ferromagnetic nanowire-loaded membranes for microwave electronics, J. Magn. Magn Mater. 321 (2009) 2055–2065, https://doi.org/10.1016/j.jmmm.2008.03.060.
[14] N. Eliaz, E. Gileadi, Induced codeposition of alloys of tungsten, molybdenum and rhenium with transition metals, in: Modern Aspects of Electrochemistry, Springer, 2008, pp. 191–301.
[15] Z. Galikova, M. Chovancova, V. Danielik, Properties of Ni-W alloy coatings on steel substrate, Chem. Pap. 60 (2006) 353–359, https://doi.org/10.2478/s11696-006-0064-2.
[16] M. Schwartz, N. Myung, K. Nobe, Electrodeposition of iron group-rare earth alloys from aqueous media, J. Electrochem. Soc. 151 (2004) C468–C477, https://doi.org/10.1149/1.1751196.
[17] M. Mulukutla, V.K. Kommineni, S.P. Harimkar, Pulsed electrodeposition of Co–W amorphous and crystalline coatings, Appl. Surf. Sci. 258 (2012) 2886–2893, https://doi.org/10.1016/j.apsusc.2011.11.002.
[18] S. Abazari, S. Rastegari, S. Kheirandish, Influence of pulse electrodeposition and heat treatment on microstructure, tribological, and corrosion behavior of nano-grain size Co-W coatings, J. Mater. Eng. Perform. 26 (2017) 3133–3143, https://doi.org/10.1007/s11665-017-2698-3.
[19] P. Bera, H. Seenivasan, K. Rajam, Studies on surface structure, morphology and composition of Co-W coatings electrodeposited with direct and pulse current using gluconate bath, Surf. Rev. Lett. 20 (2013) 1350006, https://doi.org/10.1142/S0218625x13500066.
[20] L. Yu, L. Lu, Z. Xu, J. Ma, M. Gao, X. Xu, Y. Jiang, Magnetic properties of corrosion-resistant CoW films, RSC Adv. 4 (2014) 26508–26515, https://doi.org/10.1039/c4ra02782e.
[21] G. Yar-Mukhamedova, N. Sakhnenko, T. Nenastina, Electrodeposition and properties of binary and ternary cobalt alloys with molybdenum and tungsten, Appl. Surf. Sci. 445 (2018) 298–307, https://doi.org/10.1016/j.apsusc.2018.03.171.
[22] E. Vernickaite, N. Tsyntsaru, H. Cesiulis, Electrodeposition and corrosion behaviour of nanostructured cobalt–tungsten alloys coatings, Trans. IMF 94 (2016) 313–321, https://doi.org/10.1080/00202967.2016.1220071.
[23] D. Weston, S. Gill, M. Fay, S. Harris, G. Yap, D. Zhang, K. Dinsdale, Nanostructure of Co–W alloy electrodeposited from gluconate bath, Surf. Coating. Technol. 236 (2013) 75–83, https://doi.org/10.1016/j.surfcoat.2013.09.031.
[24] N. Tsyntsaru, S. Silkin, H. Cesiulis, M. Guerrero, E. Pellicer, J. Sort, Toward uniform electrodeposition of magnetic Co-W mesowires arrays: direct versus pulse current deposition, Electrochim. Acta 188 (2016) 589–601, https://doi.org/10.1016/j.electacta.2015.12.032.
[25] N. Tsyntsaru, G. Kaziukaitis, C. Yang, H. Cesiulis, H. Philipsen, M. Lelis, J.-P. Celis, Co-W nanocrystalline electrodeposits as barrier for interconnects, J. Solid State Electrochem. 18 (2014) 3057–3064, https://doi.org/10.1007/s10008-014-2488-x.
[26] R.J. Liu, S.W. Li, X.L. Yu, G.J. Zhang, Y. Ma, J.N. Yao, B. Keita, L. Nadjo, Polyoxometalate-assisted galvanic replacement synthesis of silver hierarchical dendritic structures, Cryst. Growth Des. 11 (2011) 3424–3431, https://doi.org/10.1021/cg2001333.
[27] T. Maliar, H. Cesiulis, E.J. Podlaha, Coupled electrodeposition of Fe–Co–W alloys: thin films and nanowires, Front. Chem. 7 (2019) 542, https://doi.org/10.3389/fchem.2019.00542.
[28] A.Y. Samardak, Y.S. Jeon, S.H. Kim, A.V. Davydenko, A.V. Ognev, A.S. Samardak, Y.K. Kim, Magnetization reversal of ferromagnetic nanosprings affected by helical shape, Nanoscale 10 (2018) 20405–20413, https://doi.org/10.1039/c8nr05655b.
[29] Y.S. Jeon, S.H. Kim, B.C. Park, Y.K. Kim, Synthesis of Co nanotubes by nanoporous template-assisted electrodeposition via the incorporation of vanadyl ions, Chem. Commun. 53 (2017) 1825–1828, https://doi.org/10.1039/c6cc09843f.
[30] A. Rotaru, J.-H. Lim, D. Lenormand, A. Diaconu, J.B. Wiley, P. Postolache, A. Stancu, L. Spinu, Interactions and reversal-field memory in complex magnetic nanowire arrays, Phys. Rev. B 84 (2011) 134431, https://doi.org/10.1103/PhysRevB.84.134431.

[31] F. Béron, D. Ménard, A. Yelon, First-order reversal curve diagrams of magnetic entities with mean interaction field: a physical analysis perspective, J. Appl. Phys. 103 (2008), 07D908, https://doi.org/10.1063/1.2830955.
[32] A. Samardak, A. Ognev, A.Y. Samardak, E. Stebliy, E. Modin, L. Chebotkevich, S. Komogortsev, A. Stancu, E. Panahi-Danaei, A. Fardi-Ilkhichy, Variation of magnetic anisotropy and temperature-dependent FORC probing of compositionally tuned Co-Ni alloy nanowires, J. Alloys Compd. 732 (2018) 683–693, https://doi.org/10.1016/j.jallcom.2017.10.258.
[33] U. Admon, M. Dariel, E. Grunbaum, J. Lodder, Magnetic properties of electrodeposited Co-W thin films, J. Appl. Phys. 62 (1987) 1943–1947, https://doi.org/10.1063/1.339531.
[34] D. Tillwick, I. Joffe, Magnetic properties of Co-W alloys in relation to sintered WC-CO compacts, Scripta Metall. 7 (1973) 479–484, https://doi.org/10.1016/0036-9748(73)90099-9.
[35] K. Hüller, G. Dietz, H. Bestgen, Magnetic properties of amorphous Co75W25, J. Magn. Magn Mater. 53 (1985) 275–277, https://doi.org/10.1016/0304-8853(85)90208-2.
[36] S. Yin, Y. Wu, X. Xu, H. Wang, J. Wang, Y. Jiang, The effects of tungsten concentration on crystalline structure and perpendicular magnetic anisotropy of Co-W films, AIP Adv. 4 (2014) 127156, https://doi.org/10.1063/1.4905447.
[37] J.-J. Wang, Y. Tan, C.-M. Liu, O. Kitakami, Crystal structures and magnetic properties of epitaxial Co–W perpendicular films, J. Magn. Magn Mater. 334 (2013) 119–123, https://doi.org/10.1016/j.jmmm.2013.01.019.
[38] A. Figueroa, F. Bartolomé, J. Bartolomé, L. García, F. Petroff, C. Deranlot, F. Wilhelm, A. Rogalev, Breakdown of Hund's third rule in amorphous Co-W nanoparticles and crystalline Co3W alloys, Phys. Rev. B 86 (2012), 064428, https://doi.org/10.1103/PhysRevB.86.064428.
[39] H. Okamoto, Co-W (Cobalt-Tungsten), J. Phase Equilibria Diffus. 29 (2008), https://doi.org/10.1007/s11669-007-9229-0, 119-119.
[40] S. Komogortsev, R. Iskhakov, Law of approach to magnetic saturation in nanocrystalline and amorphous ferromagnets with improved transition behavior between power-law regimes, J. Magn. Magn Mater. 440 (2017) 213–216, https://doi.org/10.1016/j.jmmm.2016.12.145.
[41] M. Vázquez, L.G. Vivas, Magnetization reversal in Co-base nanowire arrays, Phys. Status Solidi B-Basic Solid State Phys. 248 (2011) 2368–2381, https://doi.org/10.1002/pssb.201147092.
[42] L. Vivas, M. Vazquez, J. Escrig, S. Allende, D. Altbir, D. Leitao, J. Araujo, Magnetic anisotropy in CoNi nanowire arrays: analytical calculations and experiments, Phys. Rev. B 85 (2012), 035439, https://doi.org/10.1103/PhysRevB.85.035439.
[43] M. Staño, O. Fruchart, Magnetic nanowires and nanotubes, in: Handbook of Magnetic Materials, Elsevier, 2018, pp. 155–267.
[44] R. Lavin, J. Denardin, A. Espejo, A. Cortés, H. Gómez, Magnetic properties of arrays of nanowires: anisotropy, interactions, and reversal modes, J. Appl. Phys. 107 (2010), 09B504, https://doi.org/10.1063/1.3350905.
[45] J. Fernandez-Roldan, D. Chrischon, L. Dorneles, O. Chubykalo-Fesenko, M. Vazquez, C. Bran, A comparative study of magnetic properties of large diameter Co nanowires and nanotubes, Nanomaterials 8 (2018) 692, https://doi.org/10.3390/nano8090692.
[46] A.R. Muxworthy, A.P. Roberts, First-order reversal curve (FORC) diagrams, in: D. Gubbins, E. Herrero-Bervera (Eds.), Encyclopedia of Geomagnetism and Paleomagnetism, Springer, Dordrecht, 2007, pp. 266–272.
[47] A.P. Roberts, C.R. Pike, K.L. Verosub, First-order reversal curve diagrams: a new tool for characterizing the magnetic properties of natural samples, J. Geophys. Res.-Solid Earth 105 (2000) 28461–28475, https://doi.org/10.1029/2000jb900326.
[48] E. Vilanova Vidal, Y.P. Ivanov, H. Mohammed, J. Kosel, A detailed study of magnetization reversal in individual Ni nanowires, Appl. Phys. Lett. 106 (2015), 032403, https://doi.org/10.1063/1.4906108.